© 2014. Published by The Company of Biologists Ltd | Journal of Cell Science (2014) 127, 5079–5092 doi:10.1242/jcs.159608

RESEARCH ARTICLE

A high-throughput siRNA screen identifies genes that regulate mannose 6-phosphate receptor trafficking

Mihaela Anitei[1], Ramu Chenna[1], Cornelia Czupalla[1], Milan Esner[2], Sara Christ[3], Steffi Lenhard[1], Kerstin Korn[3], Felix Meyenhofer[3], Marc Bickle[3], Marino Zerial[3] and Bernard Hoflack[1,*]

ABSTRACT

The delivery of newly synthesized soluble lysosomal hydrolases to the endosomal system is essential for lysosome function and cell homeostasis. This process relies on the proper trafficking of the mannose 6-phosphate receptors (MPRs) between the trans-Golgi network (TGN), endosomes and the plasma membrane. Many transmembrane proteins regulating diverse biological processes ranging from virus production to the development of multicellular organisms also use these pathways. To explore how cell signaling modulates MPR trafficking, we used high-throughput RNA interference (RNAi) to target the human kinome and phosphatome. Using high-content image analysis, we identified 127 kinases and phosphatases belonging to different signaling networks that regulate MPR trafficking and/or the dynamic states of the subcellular compartments encountered by the MPRs. Our analysis maps the MPR trafficking pathways based on enzymes regulating phosphatidylinositol phosphate metabolism. Furthermore, it reveals how cell signaling controls the biogenesis of post-Golgi tubular carriers destined to enter the endosomal system through a SRC-dependent pathway regulating ARF1 and RAC1 signaling and myosin II activity.

KEY WORDS: siRNA screen, Mannose 6-phosphate receptor, Post-Golgi transport, Trafficking, Lysosome

INTRODUCTION

The lysosomal degradation of endocytosed nutrients, signaling molecules and pathogens or of cytosolic components and organelles turned over by autophagy requires the proper delivery of newly synthesized, mannose 6-phosphate-tagged lysosomal hydrolases from the secretory pathway to the endosomal system. This process relies on the recycling of the mannose 6-phosphate receptors (MPRs) between the trans-Golgi network (TGN), where they bind to lysosomal hydrolases, and the endosomal system where they unload these ligands. MPRs also undergo recycling between the endosomal system and the plasma membrane, where one of the two MPRs internalizes other ligands, including insulin-like growth factor II (Ghosh et al., 2003; Munier-Lehmann et al., 1996a; Munier-Lehmann et al., 1996b). The MPRs share their trafficking routes with a number of other proteins, e.g. viral proteins (Alconada et al., 1996) or signaling receptors like Notch (Benhra et al., 2011) and Wntless (Port and Basler, 2010), which regulate cell fate and the development of multicellular organisms. Lysosomal storage disorders and bacterial pathogenesis illustrate the physiological importance of the correct delivery of newly synthesized hydrolases to the endosomal system. Mutations in proteins regulating these transport pathways have been associated with neuronal pathologies [e.g. mental retardation (Borck et al., 2008), Alzheimer's disease (Adachi et al., 2009; Mathews et al., 2002)] and neuro-muscular functions, as seen in Charcot-Marie-Tooth disease (Bucci et al., 2012), thereby showing their importance for a proper neuronal cell function during development.

Many machineries functioning in endocytosis and biosynthetic transport to the endosomal system have been described. They include coats that segregate transmembrane receptors into transport carriers while shaping membranes (McMahon and Boucrot, 2011), molecules bridging membrane and actin dynamics (Anitei et al., 2010), molecular motors for movement along F-actin and microtubules (Hirokawa et al., 2010), and the core components sustaining their fusion with target compartments (Pfeffer, 2007). Much less is known about the mechanisms that coordinate protein trafficking and organelle homeostasis in response to cell signaling during development or tissue homeostasis. Here, we have systematically silenced the kinases and the phosphatases of the human genome in order to obtain a comprehensive view of how signaling molecules control MPR trafficking.

RESULTS

siRNA-based screening identifies new regulators of MPR trafficking

To identify genes controlling MPR transport, we used HeLa cells stably expressing a chimeric protein comprising the green fluorescent protein fused to the transmembrane and cytoplasmic domain of the cation-independent mannose 6-phosphate receptor (GFP–MPR) (Waguri et al., 2003). GFP–MPR highly colocalized with the endogenous cation-independent MPR (ciMPR) in the perinuclear TGN and the more peripheral endosomal compartments. GFP–MPR also colocalized with TGN46 (also known as TGOLN2) in the perinuclear TGN (Fig. 1A–C). The steady-state distribution of GFP–MPR was used as a read-out to evaluate changes in GFP–MPR trafficking in a primary screen, in which GFP–MPR-expressing cells were transfected with small interfering RNAs (siRNAs; three siRNAs per gene, three experimental replicates) targeting each of the 710 human

[1]Biotechnology Center, Technische Universität Dresden, Tatzberg 47-51, 01307 Dresden, Germany. [2]Department of Histology and Embryology, Faculty of Medicine, Masaryk University, Kamenice 3, Building A1, 62500 Brno, Czech Republic. [3]Max Planck Institute of Molecular Cell Biology and Genetics, Pfotenhauerstrasse 108, 01307 Dresden, Germany.

*Author for correspondence (bernard.hoflack@biotec.tu-dresden.de)

Received 11 July 2014; Accepted 23 September 2014

Journal of Cell Science

Journal of Cell Science (2014) 127, 5079–5092 doi:10.1242/jcs.159608

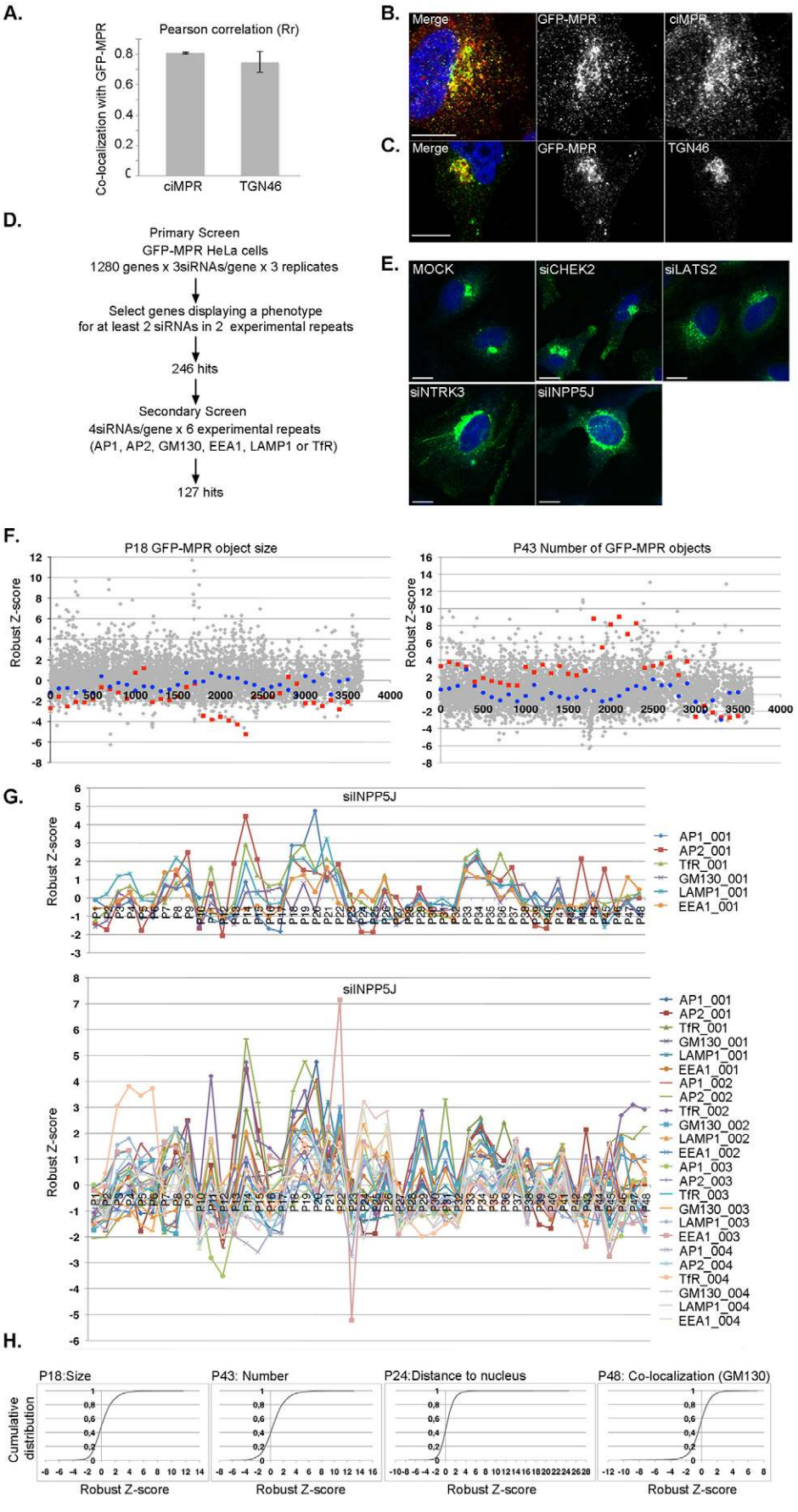

Fig. 1. (A–C) MOCK-treated GFP–MPR cells were co-labeled with (B) anti-ciMPR or (C) anti-TGN46 and analyzed by fluorescence microscopy. (A) Colocalization was analyzed by calculating the Pearson correlation coefficient (Rr) correlation, using the Volocity software (median±s.d.; $n>20$ cells per condition). (D) Scheme of the RNAi-based screens. HeLa cells stably expressing GFP–MPR were incubated with siRNAs targeting human kinases and phosphatases. Selected genes were re-tested in the secondary screen, in which cells were co-labeled with antibodies against AP-1, AP-2, GM130, LAMP1 or TfR. (E) GFP–MPR phenotypes observed in control MOCK- and RNAi-treated cells included increased GFP–MPR in the periphery (si*CHEK2*, checkpoint kinase 2), TGN fragmentation (si*LATS2*, large tumor suppressor kinase 2; si*INPP5J*), GFP–MPR tubules (si*NTRK3*) and increased GFP–MPR at the plasma membrane (si*INPP5J*). Scale bars: 10 μm. (F) Robust *Z*-scores calculated for P18 (GFP–MPR object size) and P43 (number of GFP–MPR objects) measured for all siRNAs tested in the secondary screen (gray), nocodazole-treated (red) and untreated cells (blue). Parameters P1 to P48 are described in supplementary material Fig. S2. (G) Robust *Z*-scores computed in replicate experiments for siRNAs (upper panel, siRNA 001; lower panel, siRNAs 001, 002, 003 and 004) targeting *INPP5J*. AP-1, AP-2, TfR, GM130, LAMP1 and EEA1 represent the organelle markers co-labeled in the respective conditions. (H) Distributions of robust *Z*-scores measured in the entire experiment for P18 (GFP–MPR object size), P43 (number of GFP–MPR objects), P24 (distance between GFP–MPR objects and the nucleus) and P48 (50% overlap between GFP–MPR and GM130).

Journal of Cell Science (2014) 127, 5079–5092 doi:10.1242/jcs.159608

kinases, 192 phosphatases and additional scaffolding molecules (Fig. 1D; supplementary material Table S1). As positive controls, we used siRNAs targeting known regulators of MPR transport [e.g. clathrin heavy chain (*CLTC*)] and pharmacological agents such as brefeldin A, which prevents the binding of the ARF1 GTPase to membranes and induces Golgi membrane tubulation, or nocodazole, which fragments the Golgi by preventing microtubule polymerization (supplementary material Fig. S1A,B,D). Images were analyzed to measure parameters reflecting changes in GFP–MPR distribution, i.e. the number and the size of GFP–MPR objects and their distance to the nucleus (see Materials and Methods). The hits found slightly under the threshold were examined visually. In total, we selected 246 genes for further analysis.

These 246 genes were reanalyzed in a secondary screen. GFP–MPR-expressing cells were transfected with stealth siRNAs (four siRNAs per gene, six experimental repeats) targeting each selected gene (Fig. 1D; supplementary material Table S2). Organelle morphology and integrity were analyzed by co-labeling cells with antibodies against the cis-Golgi matrix protein GM130, the transferrin receptor (TfR, which shuttles between the plasma membrane, early and recycling endosomes), the early endosome antigen 1 (EEA1), the lysosomal associated membrane glycoprotein LAMP1 (as a marker of late endosomal or lysosomal compartments), adaptor protein 1 (AP-1, a component of the clathrin coats involved in MPR sorting at the TGN) and AP-2 (a component of endocytic clathrin coats). Images were analyzed using the MotionTracking software (Collinet et al., 2010). The set of 48 parameters resulting from this analysis (described in supplementary material Fig. S2A) provided a comprehensive characterization of the fluorescent objects, i.e. GFP–MPR, nuclei and the respective organelle markers. Parameter values were normalized to control MOCK-treated cells by calculating robust *Z*-scores. The reproducibility of parameter profiles is shown for si*INPP5J* (inositol polyphosphate-5-phosphatase J), si*CLTC* and nocodazole (Fig. 1E,G; supplementary material Fig. S1E,F). Pearson correlation coefficients between the parameter values measured in the different experimental repeats (supplementary material Fig. S2B,D) validated a group of parameters measuring GFP–MPR size (P18, P19), number (P43, P45), distance to the nucleus (P24, P25) and colocalization with organelle markers (P47, P48). These parameters accurately reflected the changes in GFP–MPR distribution caused by nocodazole, but were not significantly modified in control non-treated or siNegative siRNA-treated cells (supplementary material Table S3A; Fig. 1F), and were thus chosen for hit selection. The distributions of the robust *Z*-scores calculated for P18, P43, P24 and P48 in the entire experiment are shown in Fig. 1H.

Genes were selected if at least two stealth siRNAs targeting the same gene significantly modified any of the selected parameters (supplementary material Table S3A). We selected 62 genes displaying a $|\text{median}_{\text{Robust\_Z-score}}|>1.8$, 43 genes with a $|\text{median}_{\text{Robust\_Z-score}}|$ between 1.4 and 1.8, and 14 other genes with a $|\text{median}_{\text{Robust\_Z-score}}|$ between 1.244 and 1.4 (supplementary material Table S3A). Eight genes found slightly under the threshold set for image analysis (and indicated with an asterisk in supplementary material Table S3A) were confirmed as hits by visual analysis (supplementary material Table S3B). In addition, the visual screen detected a subgroup of 11 genes whose knockdown, similar to that of *CLTC* (supplementary material Fig. S1D), caused an accumulation of GFP–MPR at the cell surface (Fig. 1E; supplementary material Table S3B). For organelle markers, changes were considered as significant if at least two stealth siRNAs showed a $|\text{robust Z-score}|\geq 2$ for any of the parameters measuring object size, number, distance to the nucleus or intensity (supplementary material Fig. S2A; Table S3A).

Phenotypic analysis

These data allowed us to analyze how the selected genes affected the co-distribution of GFP–MPR and the different organelle markers (Fig. 2A). In control cells, GFP–MPR colocalized well with AP-1 and TfR, as shown by the Pearson correlation coefficient Rr and the 50% overlap (Fig. 2B). GFP–MPR and GM130 showed a high overlap but a low Rr coefficient, consistent with their localization to adjacent but distinct Golgi subcompartments. Relatively low degrees of overlap were detected between GFP–MPR and EEA1 or LAMP1, indicating that small amounts of GFP–MPR were present at steady state in EEA1-positive early and LAMP1-positive late endosomes. Thus, our parametrical analysis was in good agreement with our previous electron microscopy studies illustrating GFP–MPR distribution (Waguri et al., 2003).

Hierarchical gene and parameter clustering analysis identified four clusters of genes affecting GFP–MPR distribution, two of them (1 and 2) characterized by changes in object number and/or distance to the nucleus, and the other two (3 and 4) by changes in object size and/or intensity (Fig. 3). Pearson correlation coefficients calculated between the parameters showed a good correlation between object size and intensity (modified in clusters 3 and 4), and object number and distribution (modified in clusters 1 and 2), respectively (supplementary material Fig. S2C). The changes observed for the genes in clusters 1 and 2 (increased GFP–MPR distance to the nucleus and/or number, and in some cases a reduced overlap between GFP–MPR and GM130) might reflect the fragmentation of the perinuclear GFP–MPR-rich compartment (TGN) or an increase in the amount of GFP–MPR in peripheral endosomes [e.g. si*FGFR1* (fibroblast growth factor receptor 1) and si*CSNK2B* (casein kinase 2, beta polypeptide) in Fig. 2A]. Visual analysis confirmed that the depletion of 63.29% of the genes in these clusters induced a dispersion of the perinuclear GFP–MPR compartment, depletion of 13.9% increased the amount of GFP–MPR in peripheral endosomes, whereas the depletion of the remaining 22.8% resulted in no apparent visual phenotype (supplementary material Table S3B). Depletion of genes in clusters 3 and 4 increased the size of GFP–MPR objects, with (cluster 3) or without (cluster 4) affecting the size and/or intensity of TfR-positive, EEA1-positive [e.g. si*PPP2R3A* (protein phosphatase 2, regulatory subunit B″ α); Fig. 2A] and/or LAMP1-positive [e.g. si*MAP3K3* (mitogen-activated protein kinase kinase kinase 3); Fig. 2A] endosomes (Fig. 3; Fig. 2D,E; supplementary material Table S3A). These genes might thus regulate the trafficking of key endosomal or lysosomal components, or the expression and/or degradation of the respective endosomal markers. A subgroup of genes affected the distribution of EEA1- and/or LAMP1-positive endosomes (Fig. 2F; supplementary material Table S3A), indicating that they modulate organelle positioning. Depletion of FGFR1, DLG3 [disks large homolog 3 (*Drosophila*)] and PIK3R5 (also known as P101-PI3K) (phosphoinositide 3-kinase, regulatory subunit 5) caused the dispersion of the TfR-positive perinuclear compartment and the fragmentation of the GM130-rich Golgi (Fig. 2D), suggesting that they maintain the integrity of the Golgi and recycling endosomes. Interestingly, a subgroup of 40 genes

Journal of Cell Science (2014) 127, 5079–5092 doi:10.1242/jcs.159608

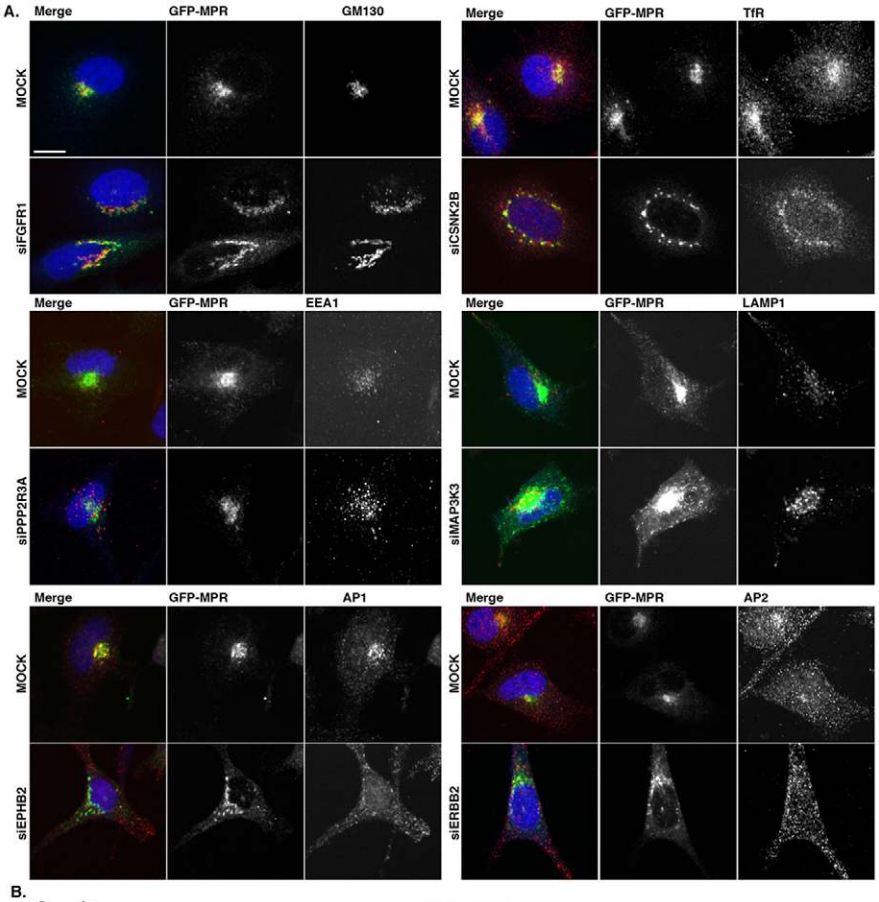

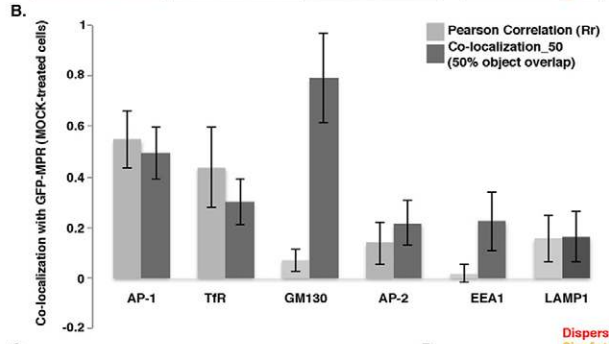

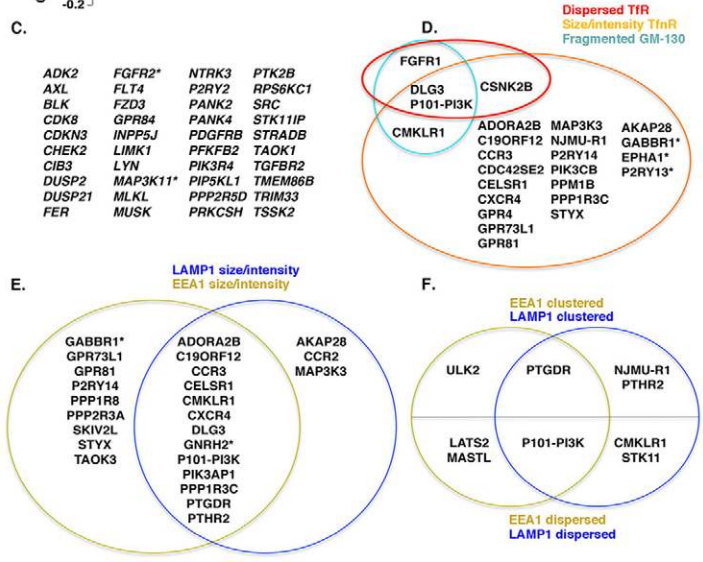

Fig. 2. Phenotypic analysis of identified kinases and phosphatases. (A) Examples of organelle distribution upon siRNA treatment in the secondary screen. siRNA-treated GFP–MPR-expressing HeLa cells were incubated with antibodies against GM130, EEA1, LAMP1, TfR, AP-1 or AP-2 (red). si*FGFR1* caused dispersion of the GFP–MPR and GM130-positive Golgi compartments, and si*CSNK2B* affected the morphology of the TfR compartment (D). si*PPP2R3A* and si*MAP3K3* caused an increase in the size and intensity of the EEA1- and LAMP1-positive objects, respectively (E). si*EPHB2* (EPH receptor B2) reduced AP-1 intensity, and si*ERBB2* affected the AP-2-positive compartment (supplementary material Table S3). Scale bar: 10 µm. (B) The colocalization (Pearson correlation coefficient Rr) and the 50% object overlap (P48) between GFP–MPR and the co-labeling organelle markers were calculated in MOCK-treated cells on a per plate basis (median±s.d.). (C–F) Genes whose depletions affected (C) only GFP–MPR or (D–F) GFP–MPR and (D) fragmentation of the TfR compartment (red), fragmentation cis-Golgi (blue) or enlargement of TfR–positive endosomes (orange); (E) enlargement of early (yellow) or late endosomes (blue); (F) clustering (reduced distance to nucleus, increased clustering) or dispersion (increased distance to nucleus) of early or late endosomes.

Journal of Cell Science (2014) 127, 5079–5092 doi:10.1242/jcs.159608

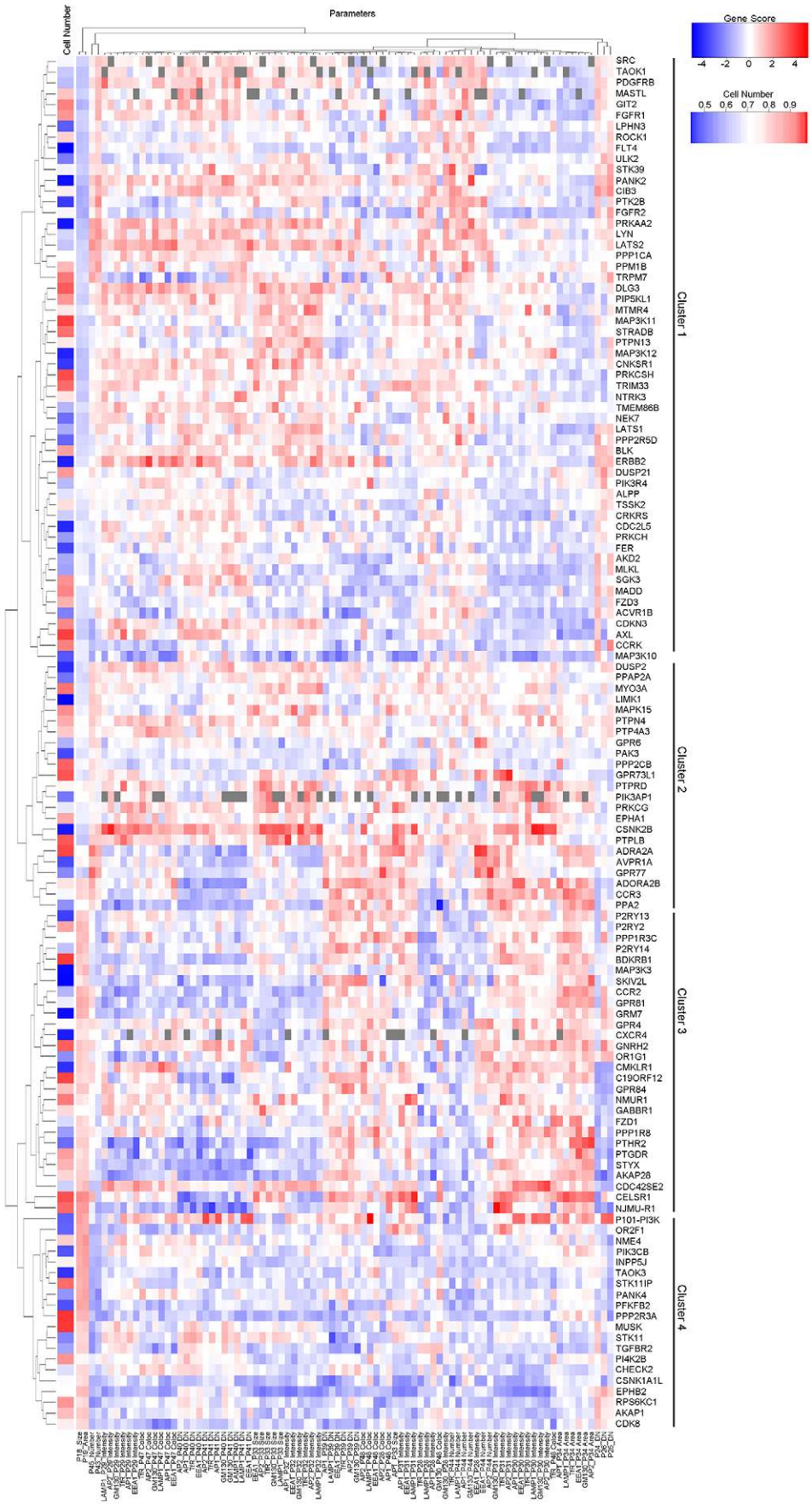

Fig. 3. Hierarchical clustering of genes whose depletion changed GFP–MPR distribution. Gene scores, calculated as the weighted average of the robust *Z*-scores of the siRNAs causing significant changes in GFP–MPR distribution (Materials and Methods), were used to compute the complete linkage hierarchical clustering of the dataset. The color key indicates the gene scores calculated for the indicated parameters. Values are color coded in the range of blue to white to red, representing low, medium and high scores, respectively, as indicated. An additional column (left) indicates median cell numbers (cell numbers were calculated as the ratios between the mean number of nuclei measured in cells treated with the respective siRNA and the mean number of nuclei in MOCK-treated cells). Values are color coded, as indicated. Clusters 1 and 2 correspond to GFP–MPR dispersion and/or an increase in the number of peripheral objects, as exemplified for si*FGFR1* and si*CSNK2B* (Fig. 2A), and clusters 3 and 4 reflect an increase in object size and/or intensity, as shown for si*MAP3K3* (Fig. 2A).

Journal of Cell Science (2014) 127, 5079–5092 doi:10.1242/jcs.159608

(Fig. 2C) exclusively affected GFP–MPR and/or AP-1 distribution, suggesting that they specifically regulate GFP–MPR trafficking and/or the homeostasis of the GFP–MPR-positive or AP-1-positive compartment.

Network analysis

Pathway analysis of the genes in clusters 1 and 2 revealed enrichment in the MAPK, focal adhesion, Wnt signaling, adherens junction and regulation of the actin cytoskeleton pathways (Fig. 4A). Cluster 3 was enriched in components of the G-protein-coupled receptor (GPCR) pathway (Fig. 4B), whereas cluster 4 was enriched in components of the phosphatidylinositol metabolism pathway (Fig. 4C).

Lipid kinases and phosphatases regulating MPR trafficking

Phosphatidylinositol phosphate (PIP) synthesis is compartmentalized along the different compartments of the secretory and the endocytic pathways, where specific PIPs are used as docking platforms by various components regulating membrane traffic (Vicinanza et al., 2008). Our screen identified five kinases and two phosphatases (Fig. 4D; supplementary material Table S3A,B). These included kinases catalyzing the synthesis of phosphatidylinositol 4-phosphate (PI-4P) on the TGN [PI4K2B (phosphatidylinositol 4-kinase type 2 beta)], phosphatidylinositol 3-phosphate (PI-3P) on early endosomes [the class III PIK3R4 (phosphoinositide-3-kinase, regulatory subunit 4)], phosphatidylinositol 4,5-bisphosphate (PI-4,5P_2) [PIP5KL1 (phosphatidylinositol-4-phosphate 5-kinase-like 1)] and phosphatidylinositol-3,4,5-trisphosphate (PI-3,4,5P_3) [class I PIK3CB (phosphatidylinositol-4,5-biphosphate 3-kinase, catalytic subunit beta), PIK3R5 and PIK3AP1 (phosphoinositide-3-kinase adaptor protein 1)]. Depletion of PI4K2B resulted in a fragmentation of the perinuclear GFP–MPR compartment, indicating a perturbation at the TGN. Depletion of the

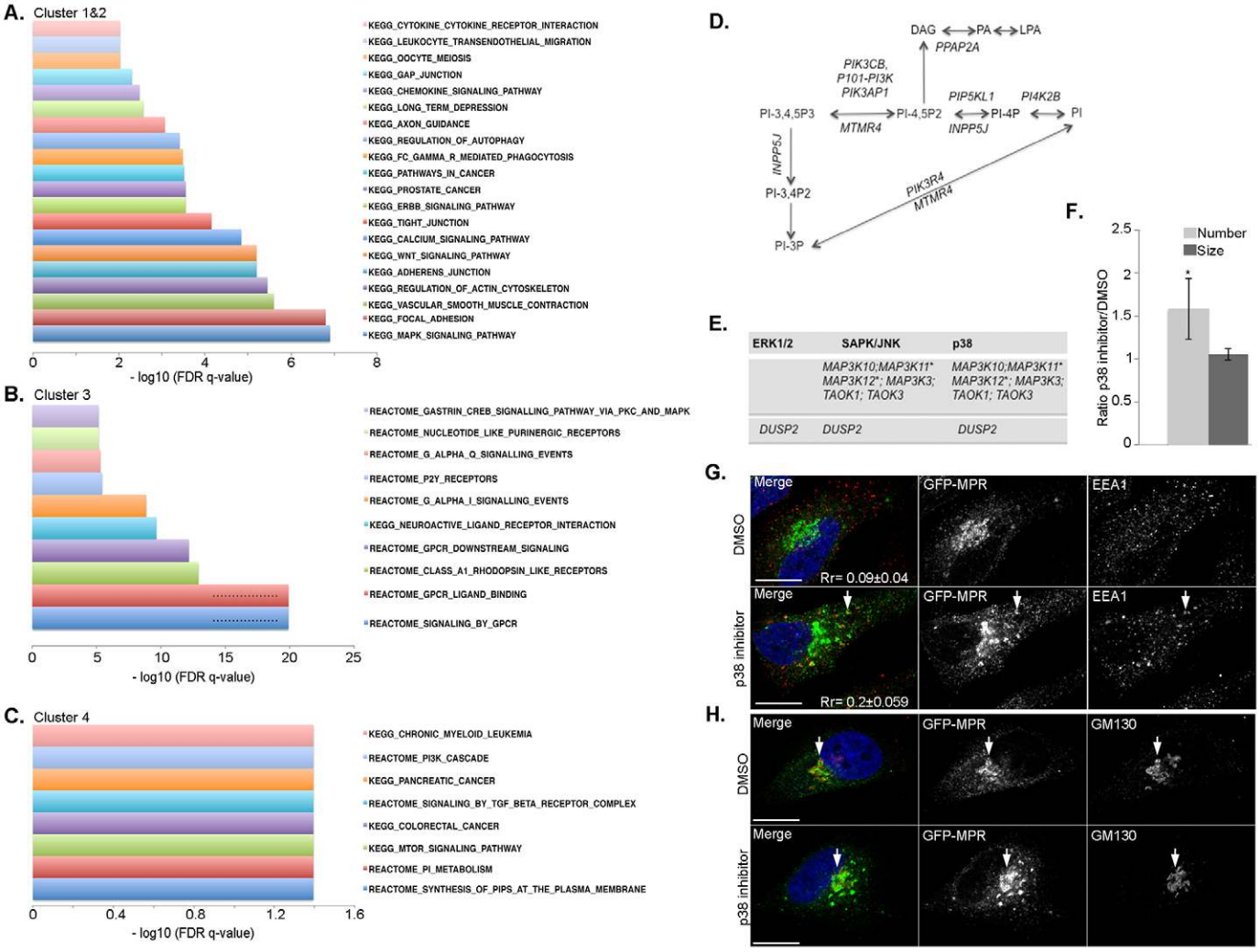

Fig. 4. Signaling pathways control GFP–MPR transport. (A–C) Pathway enrichment of the genes grouped in clusters 1 and 2 (A), cluster 3 (B) and cluster 4 (C) was calculated using the Gene Set Enrichment Analysis (GSEA) (Mootha et al., 2003; Subramanian et al., 2005). The false discovery rate (FDR) q-value was calculated for each set. (B) Dots (…) indicate a FDR q-value$<10^{-12}$. (D) Lipid-modifying enzymes and (E) components of MAPK pathways identified in the siRNA-based screen. (F–H) p38 signaling modulates GFP–MPR transport. Cells expressing GFP–MPR were incubated with DMSO or with 10 μM p38 inhibitor SB203580 for 1 h, co-labeled with antibodies against (G) EEA1 (red) or (H) GM130 (red) and then analyzed by confocal microscopy. (F) GFP–MPR object number and size (arbitrary units, a.u.) were analyzed using ImageJ. The ratios between the values measured in p38-inhibitor-treated and control DMSO-treated cells are shown (n=4 experiments, >50 cells per condition, median±s.d.; *P=0.0019, one-way ANOVA, α=0.01). Arrows indicate peripheral endosomes positive for GFP–MPR and EEA1 (G), and the Golgi (H). Scale bars: 10 μm.

Journal of Cell Science

Journal of Cell Science (2014) 127, 5079–5092 doi:10.1242/jcs.159608

3-phosphatase MTMR4 (myotubularin related protein 4) (Naughtin et al., 2010) also caused some fragmentation of the TGN. GFP–MTMR4 was detectable on EEA1-positive peripheral endosomes and on perinuclear TfR-positive structures, where it colocalized with endogenous MPR (supplementary material Fig. S3A,B), thus suggesting that MTMR4 controls MPR transport from early and recycling endosomes. Knockdown of the 5-phosphatase INPP5J, of the kinase PIK3CB or of PIK3AP1 caused the accumulation of GFP–MPR at the cell surface, indicating a perturbation of PIP metabolism at the plasma membrane and an impaired GFP–MPR endocytosis. PIP metabolism has been shown to be coupled to the production of diacylglycerol (DAG) (Sarri et al., 2011) and phosphatidic acid, two cone-shaped lipids inducing membrane curvature. Depletion of the phosphatidic acid phosphatase type 2A (PPAP2A) caused the dispersion of the perinuclear GFP–MPR compartment (Fig. 4D; supplementary material Table S3A,B). The HA-tagged PPAP2A variant 1 colocalized with GFP–MPR in the TGN (supplementary material Fig. S3C), indicating the importance of cone-shaped lipid metabolism in MPR trafficking from the TGN.

MAPK signaling pathways

Our screen also identified kinases and phosphatases of the classical MAPK pathway, particularly enriched among the genes whose depletion increased the GFP–MPR object number and/or distance to the nucleus (Fig. 4A). These included the dual-specificity phosphatase DUSP2 (dual specificity phosphatase 2), shown to control Golgi integrity (Chia et al., 2012), as well as kinases participating in the p38 and SAPK/JNK signaling cascades (Fig. 4E). To confirm that p38 signaling affected GFP–MPR transport, we used the p38 inhibitor SB203580. Compared to control, cells treated with SB203580 for 1 h exhibited a higher number of peripheral GFP–MPR objects that overlapped with EEA1 (Fig. 4F,G), but exhibited a normal Golgi morphology (Fig. 4H). This suggests that p38 signaling modulates early endosome homeostasis and GFP–MPR recycling from endosomes to the TGN.

Biogenesis of GFP–MPR tubules and actin-myosin dynamics

Genes in clusters 1 and 2 also showed a significant enrichment in components of the actin regulatory pathway (Fig. 4A). STRING analysis (Szklarczyk et al., 2011) of these genes showed that SRC (SRC proto-oncogene, non-receptor tyrosine kinase) was a major signaling hub linked to downstream actin regulatory molecules, including the ARF1 GTPase-activating protein (GAP) GIT2 (G-protein-coupled receptor kinase interacting ArfGAP 2) and the p21-activated kinase PAK3 [p21 protein (Cdc42/Rac)-activated kinase 3] (Zhang et al., 2005) (Fig. 5A). Interestingly, depletion of SRC, GIT2 or PAK3 caused a unique phenotype detected by visual analysis, i.e. an increase in the number of GFP–MPR tubules (supplementary material Table S3B). PAK3 and GIT2 are clathrin/AP-1 coat components (Baust et al., 2006) that might control RAC1-dependent actin dynamics during MPR carrier formation at the TGN (Anitei et al., 2010). Accordingly, both GFP–SRC and GFP–PAK3 were detectable on the perinuclear MPR-positive compartment (supplementary material Fig. S3D,E). Because the same phenotype (increased number of GFP–MPR tubules) was detected in cells depleted of two receptors [NTRK3 (neurotrophic tyrosine kinase, receptor, type 3) and TGFBR2 (transforming growth factor, beta receptor II 70/80 kDa)], we asked whether these receptors could affect SRC activation. Immunoprecipitation of phosphotyrosine-containing proteins showed that SRC tyrosine phosphorylation was reduced in NTRK3- but not TGFBR2-depleted cells (Fig. 5B,C), suggesting that the NTRK3 neurotrophin receptor functions upstream of SRC. To identify proteins whose tyrosine phosphorylation states were modified in SRC-depleted cells, the stable isotope labeling by amino acids in cell culture (SILAC) method was applied to both control MOCK and si*SRC*-treated cells, and phosphotyrosine-containing proteins were immunoprecipitated from these lysates. Quantitative mass spectrometry analysis of the immunoprecipitated proteins identified a group of proteins that included GIT1 (G-protein-coupled receptor kinase interacting ArfGAP 1), a PAK3 and GIT2 interactor (Bagrodia et al., 1999; Kim et al., 2003) (Fig. 5D; supplementary material Table S5). Pathway analysis of the identified proteins showed a significant enrichment in the actin cytoskeleton regulatory pathway ($-\log_{10}$ FDR q-value=5.33), supporting the hypothesis that actin dynamics was coupled to GFP–MPR tubular carrier formation. The complex containing GIT2, PAK3 and GIT1 controls myosin II activity by regulating the phosphorylation state of its regulatory light chains (MLC2) (Vicente-Manzanares et al., 2009; Zhang et al., 2005). Accordingly, we found that depletion of GIT2 or PAK3, but also SRC, TGFBR2 or NTRK3, increased the mean fluorescence intensity of Ser19-phosphorylated MLC2 (Fig. 5E; supplementary material Fig. S4A,B). When MLC2 phosphorylation was augmented by knocking down PPP1R12A (protein phosphatase 1, regulatory subunit 12A), a subunit of the MLC2 phosphatase, we also observed an increase in the number of GFP–MPR tubules (Fig. 5F,G). A similar phenotype was caused upon depletion of myosin IIA heavy chain (siMYOIIA) (supplementary material Movies 1, 3).

These myosin-II-dependent changes in tubule dynamics were comparable to those observed in cells treated with si*SRC*, si*GIT2*, si*PAK3*, si*NTRK3*, si*TGFBR2* or si*DUSP21* (dual specificity phosphatase 21), as seen by time-lapse microscopy (Fig. 6A,C; supplementary material Movies 1, 2). The same phenotype was observed in cells incubated with the TGF-β signaling inhibitor SB431542, the neurotrophin inhibitor AG879 and the SRC inhibitor 1 (but not the Rho kinase inhibitor, which caused Golgi fragmentation), thus confirming the siRNA data (Fig. 6B,C; supplementary material Fig. S4C–G). In this experiment, GFP–MPR behaved similarly to endogenous ciMPR (Fig. 6D,E) and to TGN46 in the perinuclear compartment (Fig. 6F,G), as indicated by their extent of colocalization. However, depletion of the genes that increased MPR tubule formation did not affect GFP–MPR recycling from the cell surface to endosomes and to the TGN, as measured by anti-GFP uptake (Fig. 6H,I). These data suggest that NTRK3, SRC and an actin regulatory complex containing PAK3 and GIT2 belong to a pathway that controls the dynamics of TGN-derived MPR tubules, but not retrograde MPR transport.

Our data identify a link between signals from the cell surface, actin cytoskeleton dynamics and MPR transport. Different receptors appear to regulate distinct aspects of MPR trafficking (supplementary material Table S3). To better understand these aspects, we used specific inhibitors and ligands to alter TGF-β and FGFR signaling in GFP–MPR-expressing cells. As mentioned above, si*TGFBR2* or incubation with the TGF-β signaling inhibitor SB431542 for 1 h increased the number of GFP–MPR tubular carriers forming at the TGN (Fig. 6C), without significantly affecting Golgi integrity (Fig. 6J). By contrast, incubation with the FGFR inhibitor PD173074 for 1 h caused the fragmentation of the perinuclear GFP–MPR compartment (91±14% of the cells; mean±s.d., $n=3$ experiments) (Fig. 6J), thus mimicking *FGFR1* knockdown

Journal of Cell Science (2014) 127, 5079–5092 doi:10.1242/jcs.159608

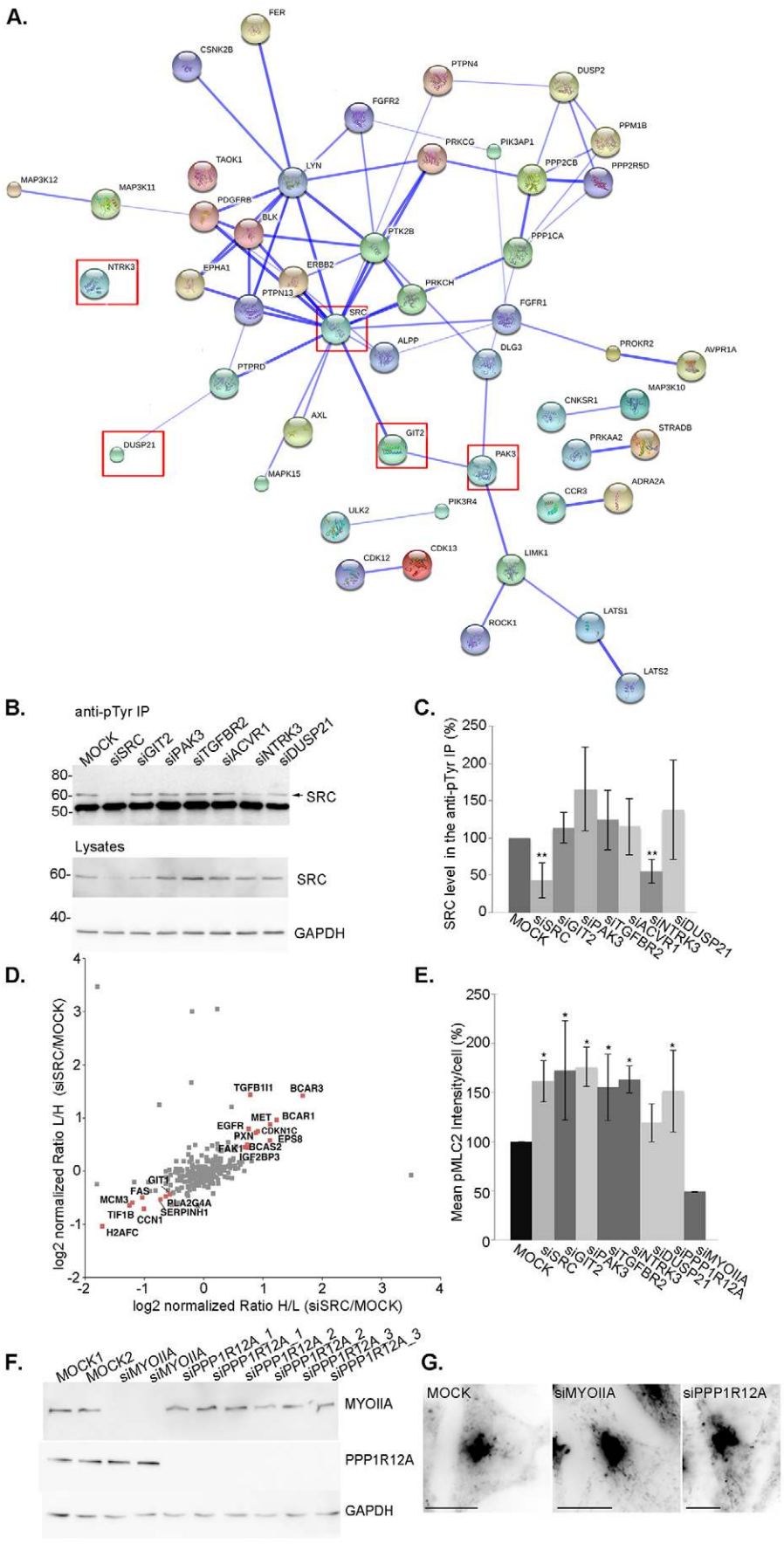

Fig. 5. Actin-myosin regulatory proteins control GFP–MPR tubular carrier biogenesis.
(A) STRING functional protein association analysis was performed for the genes found in clusters 1 and 2 (Fig. 4A). Thicker lines indicate stronger associations (STRING confidence view). SRC represents a central hub connected with signaling receptors and actin regulatory proteins. The red quadrilaterals indicate genes for which depletion caused an increase in GFP–MPR tubule formation as seen by visual analysis. (B,C) Tyrosine-phosphorylated proteins were immunoprecipitated (IP) from cell lysates with the anti-phosphotyrosine (pTyr) antibody 4G10. SRC levels in immunoprecipitates and in whole-cell lysates were analyzed by western blotting (B) and quantified (C) (median±average deviation; $n \geq 4$ experiments; $^{**}P<0.006$). (D) Quantitative mass spectrometry-based analysis of SRC substrates. Two SILAC experiments with forward and reverse labeling were performed with MOCK-transfected and si*SRC*-transfected cells. Tyrosine-phosphorylated proteins were immunoprecipitated and processed for mass spectrometry analysis. Proteins marked in red were significantly changed in abundance in both experiments ($P<0.1$). (E–G) MYOIIA controls GFP–MPR tubule dynamics. (E) Cells treated with the indicated siRNAs were labeled with anti-phospho (Ser19) MLC2 and mean fluorescence intensities per cell were measured using ImageJ (median±average deviation; $n=3$ experiments; ≥50 cells for each condition; $^{*}P<0.025$). (F) Efficiencies of siMYOIIA and si*PPP1R12A* (siRNAs 1, 2 and 3) knockdowns were evaluated by western blotting using anti-MYOIIA heavy chain, anti-PPP1R12A and anti-GAPDH as a loading control. (G) GFP–MPR-expressing (black) MOCK control, siMYOIIA and si*PPP1R12A*-treated cells were analyzed by time-lapse microscopy. Images (supplementary material Movies 1–3) were acquired every 500 ms for a total of 2 min. Images were inverted. Scale bars: 10 μm.

Journal of Cell Science (2014) 127, 5079–5092 doi:10.1242/jcs.159608

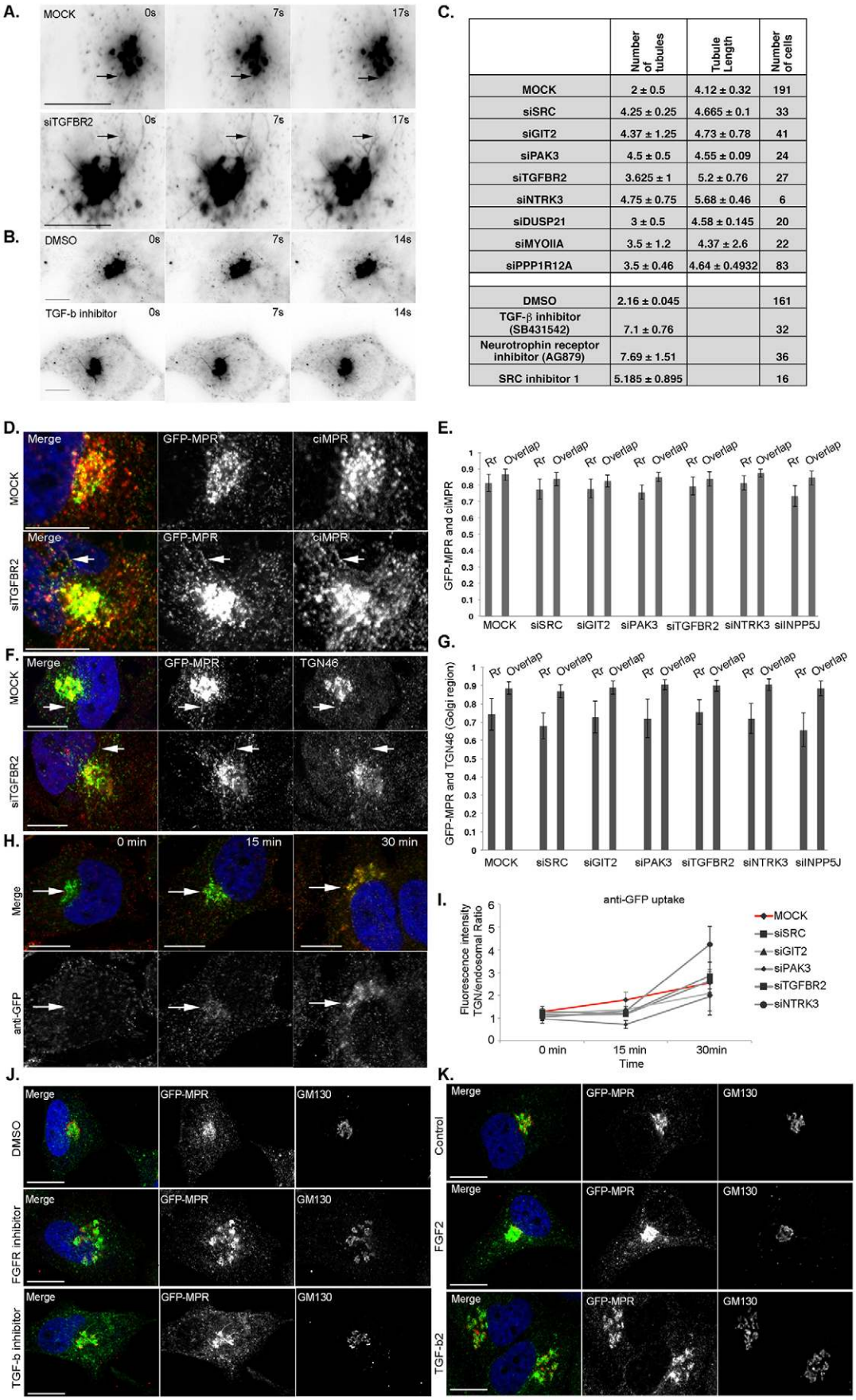

	Number of tubules	Tubule Length	Number of cells
MOCK	2 ± 0.5	4.12 ± 0.32	191
siSRC	4.25 ± 0.25	4.665 ± 0.1	33
siGIT2	4.37 ± 1.25	4.73 ± 0.78	41
siPAK3	4.5 ± 0.5	4.55 ± 0.09	24
siTGFBR2	3.625 ± 1	5.2 ± 0.76	27
siNTRK3	4.75 ± 0.75	5.68 ± 0.46	6
siDUSP21	3 ± 0.5	4.58 ± 0.145	20
siMYOIIA	3.5 ± 1.2	4.37 ± 2.6	22
siPPP1R12A	3.5 ± 0.46	4.64 ± 0.4932	83
DMSO	2.16 ± 0.045		161
TGF-β inhibitor (SB431542)	7.1 ± 0.76		32
Neurotrophin receptor inhibitor (AG879)	7.69 ± 1.51		36
SRC inhibitor 1	5.185 ± 0.895		16

Fig. 6. See next page for legend.

Fig. 6. (A,B) GFP–MPR dynamics were analyzed by time-lapse microscopy in (A) MOCK- and si*TGFBR2*-transfected or (B) DMSO- or TGFBR-inhibitor-treated cells. Images were acquired every 500 ms for a total of (A) 2 min or (B) 1 min. Images were inverted and GFP–MPR is shown in black. Arrows indicate TGN-derived GFP–MPR tubules. (C) For all indicated conditions, the number of GFP–MPR tubules forming in the TGN region and the tubule lengths were quantified (median±median absolute deviation; $n \geq 3$ experiments per condition). Images were acquired every 500 ms for a total of 2 min (siRNAs and MOCK) or 1 min (DMSO and inhibitors) (supplementary material Movies 1–3). (D–G) GFP–MPR cells co-labeled with (D) ciMPR (red) or (F) TGN46 (red) were analyzed by confocal microscopy. Arrows indicate GFP–MPR tubules emerging from the TGN. (E,G) Pearson correlation coefficients (Rr) and overlap coefficients were calculated for each condition using the Volocity software (median±s.d.; $n=3$ experiments; >20 cells per condition). (H,I) GFP–MPR-expressing cells were incubated with the respective siRNAs, and then with an antibody against GFP (red) for 1 h on ice. Cells were then incubated at 37°C for the indicated times, to allow anti-GFP uptake. Arrows indicate the TGN region. (I) Images were analyzed using ImageJ, and the ratios between the amounts of anti-GFP localized in the TGN (perinuclear GFP–MPR-positive compartment) and in the peripheral endosomal compartment were calculated (median±average deviation; $n=3$ experiments; >45 cells per condition). (J,K) Cells were (J) incubated with DMSO control, 10 μM TGFBR inhibitor or 10 μM FGFR inhibitor for 1 h, or (K) serum-starved and incubated with 10 ng/ml TGF-β2 (4 h) or 5 ng/ml FGF2 (1 h) ($n=3$ experiments; >50 cells per condition). Cells were fixed, labeled with anti-GM130 (red) and analyzed by confocal microscopy. Images were analyzed using ImageJ ($n=3$ experiments; >100 cells per condition). Scale bars: 10 μM.

(supplementary material Table S3A,B). Treatment with 10 ng/ml TGF-β2, a TGFBR ligand, for 4 h caused a fragmentation of the perinuclear GFP–MPR compartment in 70±11% of the cells, compared with 10±0.8% in control cells, as seen by confocal fluorescence microscopy (Fig. 6K). By contrast, treatment with 5 ng/ml FGF2 for 1–4 h slightly increased the size of peripheral GFP–MPR objects, without affecting the Golgi compartment (Fig. 6K). In conclusion, different signaling pathways (e.g. TGF-β and FGFR signaling) control MPR transport between the TGN and endosomes, possibly by affecting distinct regulatory steps.

DISCUSSION

Our screen illustrates how signaling pathways (represented by 127 kinases and phosphatases) control MPR trafficking. It maps the routes followed by GFP–MPR and reveals mechanisms by which cell signaling regulates post-TGN transport.

A recent kinase-inhibitor-based screen has shown that cell signaling regulates CI-MPR trafficking (Adachi et al., 2009). This study identified five kinases – a subunit of the casein kinase CK2, which is a known regulator of CI-MPR sorting (Scott et al., 2006), two catalytic subunits of the cAMP-dependent protein kinase, GSK3β and the CDC42-binding protein kinase α, which controls actin dynamics (Wilkinson et al., 2005). We confirmed a role for these signaling complexes in MPR transport by identifying a CK2 subunit (CSNK2B), a catalytic subunit of the AMP-activated protein kinase [PRKAA2 (protein kinase, AMP-activated, α2 catalytic subunit)], as well as actin regulatory proteins [CDC42SE2 (CDC42 small effector 2), LIMK1 (LIM domain kinase 1), ROCK1 (Rho-associated, coiled-coil containing protein kinase 1) and the PAK3–GIT2 complex]. At the same time, our data provide a more comprehensive view of the regulation of MPR transport.

Several siRNA-based screens have been used to study endocytosis, ER to Golgi transport or post-Golgi transport to the plasma membrane (Chia et al., 2012; Collinet et al., 2010; Farhan et al., 2010; Kozik et al., 2013; Moreau et al., 2011; Simpson et al., 2012). Among the genes identified in our screen, 47 have been shown to affect clathrin-dependent endocytosis (Collinet et al., 2010) (supplementary material Table S4), consistent with the notion that MPRs are endocytosed through clathrin-coated pits. Another 17 genes were shown to affect Golgi morphology (Chia et al., 2012; Farhan et al., 2010), and 29 genes were identified in a screen monitoring vesicular stomatitis virus glycoprotein (VSVG) secretion (Simpson et al., 2012), suggesting that MPR and VSVG trafficking share some common regulators. The latter group included receptor tyrosine kinases {e.g. AXL (AXL receptor tyrosine kinase), ERBB2 (v-erb-b2 avian erythroblastic leukemia viral oncogene homolog 2), FER, [fer (fps/fes related) tyrosine kinase], FLT4 (fms-related tyrosine kinase 4)} and cell cycle regulatory proteins [e.g. CDKN3 (cyclin-dependent kinase inhibitor 3), NEK7 (NIMA-related kinase 7), LATS1 (large tumor suppressor kinase 1), PPP2CB (protein phosphatase 2, catalytic subunit, β isozyme)] that probably control TGN homeostasis. No overlap was found with screens studying viral autophagy (Orvedahl et al., 2011) or melanogenesis (Ganesan et al., 2008). Importantly, we found 43 kinases and phosphatases not identified in the other screens that might thus specifically control MPR trafficking. These include the Golgi-localized phosphatase PPAP2A that might regulate the production of DAG from phosphatidic acid and lysophosphatidic acid (LPA) (Smyth et al., 2003), the role of which remains to be established by further studies. They also include two members of the protein kinase C family, PRKCG (protein kinase C γ) and PRKCH (protein kinase C η), which is known to regulate post-Golgi transport (Díaz Añel and Malhotra, 2005), and a group of GPCRs. Several studies have illustrated how specific G protein subunits control post-TGN carrier formation (Coria et al., 2014; Díaz Añel and Malhotra, 2005). Nevertheless, with some exceptions (Saini et al., 2010), the specific GPCRs involved in this process are not known. Here, we identify a group of 21 GPCRs that control MPR transport between TGN and endosomes. It remains to be clarified whether and how these receptors control the sorting machineries present on the TGN or endosomes.

Although it is well accepted that MPRs are in equilibrium between the TGN, endosomes and the plasma membrane, their trafficking routes, in particular those allowing their recycling back to the TGN, are not yet clear. Some studies suggest that MPRs are transported form early endosomes back to the TGN, perhaps through recycling endosomes, and others suggest that they are transported to late endosomes and then to the TGN (Anitei and Hoflack, 2012; Díaz and Pfeffer, 1998). We identified genes regulating the metabolism of PI-4P on the Golgi, PI-3P on early endosomes, PI-3,4,5P_3 on recycling endosomes (Fields et al., 2010) and PI-4,5P_2 and PI-3,4,5P_3 at the plasma membrane (Di Paolo and De Camilli, 2006; Vicinanza et al., 2008). Although we cannot exclude the possibility that our GFP–MPR reporter and the full-length MPR follow slightly different routes (Barbero et al., 2002; Waguri et al., 2006), our screen would be consistent with the recycling of MPRs from early endosomes to the TGN, possibly along a retromer-dependent (Arighi et al., 2004; Lin et al., 2004; McKenzie et al., 2012; Popoff et al., 2007; Wassmer et al., 2007) or an AP-1-dependent (Hirst et al., 2012; Meyer et al., 2000) sorting pathway.

This study provides a comprehensive view of how signaling regulates MPR trafficking. Several signaling cascades regulating key aspects of cell homeostasis (cell adhesion, actin dynamics) or development of multicellular organisms (TGF-β signaling, Wnt/β-catenin) modulate MPR transport or the homeostasis of the

Journal of Cell Science (2014) 127, 5079–5092 doi:10.1242/jcs.159608

compartments that these receptors encounter. Receptor tyrosine kinases, GPCRs, TGF-β and neurotrophin receptors appear to regulate distinct stages of the transport between the TGN and endosomes. Interestingly, NTRK3 and TGFBR2 regulate the formation of tubular carriers mediating the MPR sorting at the TGN. The NTRK3 signaling cascade includes SRC and the ARF1 GAP GIT1, which together with GIT2, PAK3 and the RAC1 guanine exchange factor (GEF) β-PIX (ARHGEF7) form a complex central for the sorting function of clathrin/AP-1 coats mediating MPR trafficking (Anitei et al., 2010; Baust et al., 2006). This module controls myosin II activity through the phosphorylation of its light chain, as also seen in neurons (Zhang et al., 2005). Myosin light chain phosphorylation increases the formation of stable actomyosin filaments (Vicente-Manzanares et al., 2009). Actin filaments might facilitate tubule elongation by reducing the threshold density of molecular motors required to deform the TGN membrane, as seen for myosin 1b (Yamada et al., 2014). Alternatively, myosin light chain phosphorylation might reduce myosin II turnover and decrease the available pool of myosin II (Watanabe et al., 2007) regulating clathrin/AP-1 carrier biogenesis. Myosin II might have additional effects on Golgi homeostasis, because it also modulates Rab6-dependent retrograde and anterograde transport (Miserey-Lenkei et al., 2010).

PAK3, GIT1, GIT2 and the AP-1s subunit are essential for neuronal circuit development and cognitive functions, because mutations in the corresponding genes are associated with mental retardation (Allen et al., 1998; Fiuza et al., 2013; Tarpey et al., 2006). This pathology might illustrate the importance of the clathrin/AP-1-dependent transport of selected neuronal receptors (Farías et al., 2012; Margeta et al., 2009). Neurotrophins are known to regulate neural circuit development and function (Park and Poo, 2013). Our screen shows that neurotrophin signaling modulates clathrin/AP-1-dependent transport and actin-myosin dynamics through a SRC-, PAK3- and GIT1/2-dependent pathway, and most likely identifies key components involved in synaptogenesis and neuronal plasticity. By identifying genes regulating the fine-tuning of trafficking between the TGN and endosomes, our screen might contribute to a better understanding of key aspects of neuronal development and its associated pathology.

MATERIALS AND METHODS

Antibodies and constructs

The antibodies used in this study were as follows: mouse antibodies against AP-1γ, AP-2α, LAMP-1, GM130, EEA1, GIT1 and GIT1/2 (BD Biosciences, NJ), mouse antibody against transferrin receptor (Zymed, Invitrogen, Life Technologies, Germany), mouse anti-phosphotyrosine (4G10 clone, made in-house or obtained from EMD Millipore, Merck, Germany), anti-GAPDH (Abnova, Taiwan), anti-SRC (L4A1, Cell Signaling Technology, New England Biolabs, Germany), anti-HA (Max Planck Institute of Molecular Cell Biology and Genetics, Dresden, Germany) and anti-GFP (Roche Diagnostics, Germany); rabbit antibodies against SRC (32G6), myosin light chain 2, phospho-myosin light chain 2 (Ser19), myosin IIA heavy chain (Cell Signaling), and ciMPR (made in-house); sheep anti-TGN46 (Novus Biologicals, Germany). The secondary antibodies used were Alexa-Fluor-647-conjugated anti-mouse-IgG (1:1000 for the screen for AP-2α, LAMP-1, GM130 and EEA1), Alexa-Fluor-546-conjugated goat anti-mouse-IgG (1:200 for AP-1γ in the screen; 1:400 for other immunostainings), Alexa-Fluor-488-conjugated goat anti-mouse-IgG, Alexa-Fluor-594-conjugated and Alexa-Fluor-488-conjugated goat anti-rabbit-IgG as well as phalloidin–Alexa-Fluor-546 (Molecular Probes, Invitrogen, Life Technologies). The plasmids used were RFP-tagged ciMPR (Waguri et al., 2003), HA-tagged PPAP2A variant 1 (Roberts et al., 1998), MTMR4-GFP (Thomas Wassmer, UK), PAK3-GFP (Kreis et al., 2007) and GFP-tagged chicken SRC WT (Giulio Superti-Furga, Austria).

Stealth siRNAs

The Stealth siRNAs (Invitrogen, Life Technologies) used for additional experiments were as follows: PAK3, 5′-AAAGCUUGCAGGCA-CUCUCUGCAGA-3′; GIT2, 5′-UGGAGUUGCUUGCUAAGAUC-UUUGG-3′; SRC, 5′-CAGCAGCUGGUGGCCUACUACUCCA-3′; TGFBR2, 5′-GCAGAAGCUGAGUUCAACCUGGGAA-3′; ACVR1, 5′-CCAGCUGUGGUUAAUUACACAUUAU-3′; NTRK3, 5′-CCAUU-UGCGUUAUAUAAACCUGUCA-3′; DUSP21, 5′-UAUCGAUGGU-GUGGAUAAGAUCAGC-3′; PPP1R12A (NM_002480.1) siRNA 1 (HSS106921), 5′-GCUUGCAUAUGUUGCACCUACAAUA-3′; siRNA 2 (HSS106922), 5′-GGGUUGAUAUAGAAGCAGCUCGAAA-3′; siRNA 3 (HSS181423), 5′-CAAAGUGGGCCAAACAGCCUUUGAU-3′; Myosin IIA heavy chain (NM_002473.4; MYH9) stealth 541, 5′-UGUAGAUGAGCCCUGAGUAGUAACG-3′.

RNAi-based screening

For the primary screen, HeLa cells stably expressing GFP–MPR were reverse-transfected with 10 nM siRNA and 0.06 µl of INTERFERin (Polyplus Transfection, France) per well in 384-well plates (CellCarrier, Perkin Elmer). 1000 cells in 50 µl of DMEM (Invitrogen, Life Technologies) with 10% FCS (Roth), penicillin-streptomycin (Gibco, Invitrogen, 15140) and 100 µg/ml Geneticin 418 (1:500) were plated in each well. We used an Ambion Kinase/Phosphatase V2 library containing three siRNAs per gene (Ambion, Life Technologies, Germany) (supplementary material Table S1A), and the screen was repeated three times. Each plate contained controls for transfection efficiency (*Eg5*, *GFP*), negative controls [untransfected, MOCK (incubated with Interferin), siAllstar (used for normalization in the primary screen), siSilencer6] and positive siRNA controls (si*CLTC*, si*AP3M1*, si*SNX5B*, si*PI4K2A*). In addition, cells were treated with chemical inhibitors known to modify MPR localization, including 10 µg/ml brefeldin A (Sigma-Aldrich) for 30 min or 10 µm nocodazole (Calbiochem) for 1 h. The general plate layout is shown in supplementary material Fig. S1A. Cells were fixed at 72 h after transfection by adding 50 µl of formaldehyde per well (3.7% final concentration) for 10 min at room temperature. Plates were next washed with PBS. At 0–1 days before image acquisition, plates were labeled with 30 µl of solution containing 1 µg/ml DAPI and 0.2 µM SYTO®42Blue Fluorescent Nucleic Acid Stain (Invitrogen, Life Technologies) and incubated for 60 min at room temperature, then washed with PBS. 50 µl of 0.1% sodium azide in PBS was added to each plate before storing them at 4℃.

In the secondary screen, cells were plated in 384-well plates (CellCarrier, Perkin Elmer) in 40 µl of medium per well, and transfected with 10 nM Stealth siRNAs (four siRNAs per gene; Invitrogen Stealth siRNA library, supplementary material Table S2A); 0.15 µl of INTERFERin diluted 1:5 in Ambion nuclease-free water was added to each well. In each plate, there were transfection controls (*Eg5*), negative controls [untransfected cells, non-targeting Stealth siRNA-treated cells and MOCK-treated cells (INTERFERin only)]. MOCK-transfected cells were used for normalization. As positive controls we used si*AP3M1*, si*CLTC* and si*PI4K2A*, as well as brefeldin A and nocodazole. Cells were then fixed by adding 50 µl of formaldehyde (final concentration 3.7%), washed, permeabilized with 0.1% Triton X-100 in PBS for 5 min, washed and blocked with 3% bovine serum albumin (BSA) in PBS for 20 min. Cells were then incubated with primary antibodies for 1 h at room temperature, washed, incubated with the corresponding secondary antibodies and washed before 1 µg/ml DAPI (nuclear dye) and 3 µg/ml HCS Cell Mask Blue (cytoplasmic/nuclear dye, Invitrogen, Life Technologies) were added with 0.02% sodium azide (final concentration). Plates were sealed and stored at 4℃ until acquisition. Transfection efficiencies in the primary and secondary screens were 85±25% and 80±9% (mean±s.d.), respectively (supplementary material Fig. S1C).

Journal of Cell Science (2014) 127, 5079–5092 doi:10.1242/jcs.159608

Image acquisition

Image acquisition was performed using an OPERA (Evotec Technologies-PerkinElmer, MA) spinning disk microscope with laser-based autofocus, and a 40× NA 0.9 water-immersion objective. A total of 15 fields were collected for each well, with the 405-nm and 488-nm lasers for the primary screen or 405-nm, 488-nm and 647-nm or 561-nm lasers for the secondary screen. Images were corrected, analyzed and filtered (out of focus images, number of nuclei ≥ 3, number of GFP objects ≥ 10, intensity of nuclear staining) using the MotionTracking software as described previously (Collinet et al., 2010) (primary and secondary screen) and using Cell Profiler (Kamentsky et al., 2011) (primary screen). For each image, all the objects inside the cell area (identified with HCS Cell Mask Blue) were detected and analyzed using parameters describing object intensity, number, size and distribution (Collinet et al., 2010). The number of objects per cell was calculated by dividing the number of objects by the number of nuclei. Calculated distances between objects and nuclei were normalized to the mean area of the nuclei/π. Colocalization was calculated as the relative population of objects in a channel that had >50% or 66.6% volume overlap with an object in another channel. Random colocalization was estimated by automatically scrambling (five permutations) the pixels of the respective image. Colocalization was then corrected by subtracting random colocalization as follows: colocalization corrected=(colocalization$_{measured}$ − colocalization$_{random}$)/(1 − colocalization$_{random}$) (Collinet et al., 2010).

Transfection efficiency was calculated for each plate as 100−[mean(number of nuclei$_{Eg5}$)/mean(number of nuclei$_{MOCK}$)]. All siRNAs that showed a mean(number of nuclei$_{siRNA}$)/mean(number of nuclei$_{MOCK}$) ≤ 0.4 were considered toxic. All genes for which more than two siRNAs were toxic were excluded from further analysis (311 genes; 24% of total). Additional data were excluded when out-of-focus images or a lack of concordance between the phenotypes for the siRNAs targeting the same gene were observed.

Data normalization and hit selection

Images were analyzed using MotionTracking software (Collinet et al., 2010) (primary and secondary screen) and Cell Profiler (Kamentsky et al., 2011) (primary screen). Data was normalized on a per plate basis (1) in the primary screen relative to MOCK-treated cells (210 images=15 fields×14 wells in each plate) or Allstar control siRNA-treated cells (60 images=15 fields×4 wells per plate), and (2) in the secondary screen, relative to MOCK values (135 images=15 fields×9 wells in each plate) calculated per plate. The normalization was performed by calculating the robust Z-score=(median$_{siRNA}$−median$_{MOCK}$)/median absolute deviation$_{MOCK}$ (resilient to outliers). In the primary screen, genes were selected for further analysis if transfection with two of the three siRNAs resulted in similar phenotypes in two of the three replicate experiments. In the secondary screen, genes were selected as hits (1) if, for any of the validated parameters for GFP–MPR, the |median(Robust Z score$_{siRNA}$)| ≥ 1.25 or (2) if transfection with at least two Stealth siRNAs led to similar visual phenotypes in at least four of the six replicates. For co-labeling markers, a kinase or phosphatase was selected as a hit if any of the validated parameters showed a |Robust Z score$_{siRNA}$| ≥ 2 for at least two siRNAs. The statistical and data analysis procedures were carried out with Python 2.6.5 and R 2.15.1 programming languages. A pipeline was developed with C-Shell script to automate the various steps, and the plots were generated through R language. The underlying operating system was Linux.

Gene clustering

To normalize for inter-plate variation, a plate constant Wk was calculated (König et al., 2007) as follows: Wk=|(median$_{nocodazole}$−median$_{MOCK}$)/(average deviation$_{nocodazole}$−average deviation$_{MOCK}$)|, where nocodazole is the positive control and MOCK is the negative control. For each selected parameter in each replicate, we calculated a Gene Score=[$\sum_{j=1-n}$ Wk$_j$×Robust Z-score (siRNA$_j$)]/($\sum_{j=1-n}$Wk$_j$), where n represents included siRNAs (i.e. the siRNAs for which the |Robust Z-score| ≥ 1.25 for any of the parameters measuring GFP–MPR. Gene Scores were used for hierarchical clustering with complete linkage (provided by R programming library) to find similar gene clusters.

Pathway enrichment analysis

Pathway enrichment analysis was performed using Gene Set Enrichment Analysis (http://www.broadinstitute.org/gsea/msigdb/annotate.jsp), based on the Kyoto Encyclopedia of Genes and Genomes (KEGG) and Reactome (GO) databases. Protein interactions were analyzed using Search Tool for the Retrieval of Interacting Genes/Proteins (STRING) (Snel et al., 2000) and the Human Protein Reference Database (HPRD) (Prasad et al., 2009). Gene expression in HeLa cells according to different databases [Human Protein Reference Database, EMBL-EBI, Pubmed, Ambion validation by PCR, proteomic analysis (Geiger et al., 2012)] or antibody datasheets as provided by various companies is shown in supplementary material Table S3B.

Real-time microscopy

GFP–MPR-expressing cells were plated on round 35-mm, No 1.5 glass-bottomed plates (MatTek Corporation, MA) and transfected with the indicated siRNAs (10 nM) and INTERFERin. Cells were also incubated with the following inhibitors or growth factors: neurotrophin inhibitor AG879 (10 µM, 1 h incubation), TGF-β signaling inhibitor SB431542 (10 µM, 1 h; Sigma-Aldrich, Germany), the Rho kinase inhibitor (10 µM, 2 h), the p38 inhibitor SB203580 (10 µM, 1 h) and SRC inhibitor 1 (10 µM, 1 h; Millipore/Calbiochem, Germany), the FGFR1 inhibitor PD173074 (10 µM, 1 h; Selleckchem, Germany), FGF2 (5 ng/ml, 1–4 h; Miltenyi Biotec, Germany) or TGF-β2 (10 ng/ml, 4 h; Agrenvec, Spain). Before growth factor stimulation, cells were starved for 3 h in DMEM containing 0.1% BSA. Cells were analyzed at 37℃, 5% CO_2 with a Zeiss Axiovert 200-4D microscope equipped with a CCD Coolsnap HQ camera and a Zeiss Plan-Apochromat 63× 1.4 NA oil or a Zeiss C-Apochromat 63× 1.2 NA water objective (Zeiss, Germany). Images were acquired every 0.5 s for 2 min (siRNAs) or 1 min (inhibitors) and analyzed using Metamorph (Molecular Devices, CA) and ImageJ softwares.

Immunofluorescence and confocal microscopy

Cells were transfected with the indicated siRNAs (10 nM, 72 h), fixed with 4% paraformaldehyde for 15 min at room temperature, permeabilized with 0.1% Triton X-100 for 5 min at room temperature, blocked with 3% BSAe (BSA) and labeled with the primary (1 h) and then secondary (20 min) antibodies. Images were acquired with a Zeiss Laser Scanning 780 confocal microscope and Zeiss Plan-Apochromat 63× 1.4 NA, or 100× 1.4 NA oil-immersion objectives and analyzed with ImageJ or Cell Profiler (Carpenter et al., 2006). Where indicated, colocalization was measured using the Volocity Software (PerkinElmer, MA). For anti-GFP uptake, GFP–MPR-expressing cells were incubated with an antibody against GFP (1:200 in DMEM with 10% FCS) and allowed to bind it for 1 h on ice, and then incubated at 37℃ for the indicated times to allow anti-GFP uptake. Fixed cells were analyzed by confocal microscopy, and the amounts of anti-GFP localized in the TGN and in the peripheral compartment were analyzed using ImageJ.

Immunoprecipitation

Cells grown in 10-cm dishes and incubated with the indicated siRNAs (20 nM, 72 h) were collected in lysis buffer (1% NP-40, 25 mM Tris-HCl pH 7.4, 150 mM NaCl, 5 mM EDTA, 2 mM $MgCl_2$) with 2 mM sodium orthovanadate, 8 mM NaF, 2 mM sodium pyrophosphate, 5 mM β-glycero-phosphate, 1 mM phenylmethylsulfonyl fluoride (PMSF) (all from Sigma-Aldrich, Germany) and complete protease inhibitors (Roche, Germany), and lysed by passing 20 times through a 27G needle and incubated for 30 min on ice. Post-nuclear supernatants obtained after centrifugation (5 min, 5000 ***g***, 4℃) were either subjected to SDS-PAGE and western blotting to analyze protein levels, or precleared with 60 µl of protein-A–Sepharose beads (50% suspension) for 30 min at 4℃, with rotation. Precleared lysates were

incubated with anti-phosphotyrosine antibodies (4G10) coupled to protein-A–Sepharose beads (GE Healthcare, Sweden) or 4G10 Platinum anti-phosphotyrosine Agarose Conjugate (Millipore, CA) for 4 h at 4℃, with rotation. Beads were washed five times with lysis buffer, resuspended in 20 µl of 4× Laemmli buffer and analyzed by SDS-PAGE and western blotting.

SILAC labeling and cell culture

For SILAC experiments, HeLa cells were cultured in DMEM (4.5 g/l glucose)-based medium supplemented with 10% (v/v) dialyzed fetal calf serum (FCS). Arg-6/Lys-6 'heavy' and Arg-0/Lys-0 'light' SILAC media were prepared by adding L-$^{13}C_6$-arginine and L-$^{13}C_6$-lysine (Cambridge Isotope Laboratories, Andover, MA) or the corresponding non-labeled amino acids, respectively, and cells were cultured for 7–14 days in SILAC medium. Immunoprecipitation of tyrosine-phosphorylated proteins was performed as described above.

Mass spectrometry

In-gel tryptic digests and peptide extraction were performed as described previously (Czupalla et al., 2006). Peptides were separated on an UltiMate3000 nanoHPLC system (Dionex, Amsterdam, The Netherlands) equipped with a PepMap C18 nano trap column (3 µm, 100 Å, 2 cm×75 µm internal diameter) and a PepMap C18 analytical column (3 µm, 100 Å, 15 cm×75 µm internal diameter) directly coupled to the nanoelectrospray source (Proxeon, Odense, Denmark) of a LTQ Orbitrap XL mass spectrometer (Thermo Fisher Scientific, Bremen, Germany). Peptides were eluted with an 80-min linear gradient of 5–45% acetonitrile in 0.1% formic acid at 200 nl/min. Mass spectra were acquired in a data-dependent mode with one MS survey scan (resolution of 60,000) in the Orbitrap and MS/MS scans of the eight most intense precursor ions in the LTQ. Data analysis was performed using MaxQuant version 1.2.0.11 (Cox and Mann, 2008). Peak lists were searched against a database containing 20,253 entries from the UniProt-KB/Swiss-Prot human database (release 2011_02) and 255 frequently observed contaminants as well as reversed sequences of all entries and the following search criteria: (1) enzyme specificity, trypsin; (2) mass accuracy, 6 ppm and 0.5 Da for precursor ion and fragment ion mass tolerance, respectively; (3) fixed and variable modifications, cysteine carbamidomethylation and methionine oxidation, respectively; (4) maximum of two missed cleavage sites. Peptide identifications were accepted based on their posterior error probability until <1% reverse hits were retained, while protein false discovery rates were <1%. Proteins were considered if at least two peptides were identified. Protein quantification was performed by MaxQuant based on the median SILAC ratios of at least two peptides per sample. Results were only included if the experiment-to-experiment variation of protein ratios was <30% in two independent experiments with SILAC label swapping.

Acknowledgements

We thank Andrew Morris (University of Kentucky College of Medicine, Lexington, KY) for HA–PPAP2A, Thomas Wassmer (Aston University, UK) for MTMR4–GFP and Jean-Vianney Barnier (CNRS-Université Paris-Sud, France) for PAK3–GFP. We thank lab members for their helpful discussions and critical comments and Theresia Pursche (Technische Universitaet Dresden, Germany) for technical assistance.

Competing interests

The authors declare no competing interests.

Author contributions

M.A. designed, performed and analyzed the experiments. R.C. did the data analysis with M.A. C.C. designed, performed and analyzed the SILAC experiments together with S.L. and M.A. M.B., M.E., S.C., K.K., F.M. and M.Z. performed the screen, the automated image acquisition and analysis. B.H. designed and analyzed experiments, and wrote the manuscript with M.A.

Funding

Our research was supported in part by grants from Deutsche Forschungsgemeinschaft [grant numbers TRR 83/1-2010, HO 2584/1-1, HO 2584/2-1, HO 2584/6-1, HO 2584/8-1 and HO 2584/9-1]; and TU-Dresden. R.C. is funded by European Structural Funds [grant number EFRE 301270 UT 135].

Supplementary material

Supplementary material available online at
http://jcs.biologists.org/lookup/suppl/doi:10.1242/jcs.159608/-/DC1

References

Adachi, A., Kano, F., Saido, T. C. and Murata, M. (2009). Visual screening and analysis for kinase-regulated membrane trafficking pathways that are involved in extensive beta-amyloid secretion. *Genes Cells* **14**, 355-369.
Alconada, A., Bauer, U. and Hoflack, B. (1996). A tyrosine-based motif and a casein kinase II phosphorylation site regulate the intracellular trafficking of the varicella-zoster virus glycoprotein I, a protein localized in the trans-Golgi network. *EMBO J.* **15**, 6096-6110.
Allen, K. M., Gleeson, J. G., Bagrodia, S., Partington, M. W., MacMillan, J. C., Cerione, R. A., Mulley, J. C. and Walsh, C. A. (1998). PAK3 mutation in nonsyndromic X-linked mental retardation. *Nat. Genet.* **20**, 25-30.
Anitei, M. and Hoflack, B. (2012). Bridging membrane and cytoskeleton dynamics in the secretory and endocytic pathways. *Nat. Cell Biol.* **14**, 11-19.
Anitei, M., Stange, C., Parshina, I., Baust, T., Schenck, A., Raposo, G., Kirchhausen, T. and Hoflack, B. (2010). Protein complexes containing CYFIP/Sra/PIR121 coordinate Arf1 and Rac1 signalling during clathrin-AP-1-coated carrier biogenesis at the TGN. *Nat. Cell Biol.* **12**, 330-340.
Arighi, C. N., Hartnell, L. M., Aguilar, R. C., Haft, C. R. and Bonifacino, J. S. (2004). Role of the mammalian retromer in sorting of the cation-independent mannose 6-phosphate receptor. *J. Cell Biol.* **165**, 123-133.
Bagrodia, S., Bailey, D., Lenard, Z., Hart, M., Guan, J. L., Premont, R. T., Taylor, S. J. and Cerione, R. A. (1999). A tyrosine-phosphorylated protein that binds to an important regulatory region on the cool family of p21-activated kinase-binding proteins. *J. Biol. Chem.* **274**, 22393-22400.
Barbero, P., Bittova, L. and Pfeffer, S. R. (2002). Visualization of Rab9-mediated vesicle transport from endosomes to the trans-Golgi in living cells. *J. Cell Biol.* **156**, 511-518.
Baust, T., Czupalla, C., Krause, E., Bourel-Bonnet, L. and Hoflack, B. (2006). Proteomic analysis of adaptor protein 1A coats selectively assembled on liposomes. *Proc. Natl. Acad. Sci. USA* **103**, 3159-3164.
Benhra, N., Lallet, S., Cotton, M., Le Bras, S., Dussert, A. and Le Borgne, R. (2011). AP-1 controls the trafficking of Notch and Sanpodo toward E-cadherin junctions in sensory organ precursors. *Curr. Biol.* **21**, 87-95.
Borck, G., Mollà-Herman, A., Boddaert, N., Encha-Razavi, F., Philippe, A., Robel, L., Desguerre, I., Brunelle, F., Benmerah, A., Munnich, A. et al. (2008). Clinical, cellular, and neuropathological consequences of AP1S2 mutations: further delineation of a recognizable X-linked mental retardation syndrome. *Hum. Mutat.* **29**, 966-974.
Bucci, C., Bakke, O. and Progida, C. (2012). Charcot-Marie-Tooth disease and intracellular traffic. *Prog. Neurobiol.* **99**, 191-225.
Carpenter, A. E., Jones, T. R., Lamprecht, M. R., Clarke, C., Kang, I. H., Friman, O., Guertin, D. A., Chang, J. H., Lindquist, R. A., Moffat, J. et al. (2006). CellProfiler: image analysis software for identifying and quantifying cell phenotypes. *Genome Biol.* **7**, R100.
Chia, J., Goh, G., Racine, V., Ng, S., Kumar, P. and Bard, F. (2012). RNAi screening reveals a large signaling network controlling the Golgi apparatus in human cells. *Mol. Syst. Biol.* **8**, 629.
Collinet, C., Stöter, M., Bradshaw, C. R., Samusik, N., Rink, J. C., Kenski, D., Habermann, B., Buchholz, F., Henschel, R., Mueller, M. S. et al. (2010). Systems survey of endocytosis by multiparametric image analysis. *Nature* **464**, 243-249.
Coria, A. S., Masseroni, M. L. and Díaz Añel, A. M. (2014). Regulation of PKD1-mediated Golgi to cell surface trafficking by Gαq subunits. *Biol. Cell* **106**, 30-43.
Cox, J. and Mann, M. (2008). MaxQuant enables high peptide identification rates, individualized p.p.b.-range mass accuracies and proteome-wide protein quantification. *Nat. Biotechnol.* **26**, 1367-1372.
Czupalla, C., Mansukoski, H., Riedl, T., Thiel, D., Krause, E. and Hoflack, B. (2006). Proteomic analysis of lysosomal acid hydrolases secreted by osteoclasts: implications for lytic enzyme transport and bone metabolism. *Mol. Cell. Proteomics* **5**, 134-143.
Di Paolo, G. and De Camilli, P. (2006). Phosphoinositides in cell regulation and membrane dynamics. *Nature* **443**, 651-657.
Díaz, E. and Pfeffer, S. R. (1998). TIP47: a cargo selection device for mannose 6-phosphate receptor trafficking. *Cell* **93**, 433-443.
Díaz Añel, A. M. and Malhotra, V. (2005). PKCeta is required for beta1gamma2/beta3gamma2- and PKD-mediated transport to the cell surface and the organization of the Golgi apparatus. *J. Cell Biol.* **169**, 83-91.
Farhan, H., Wendeler, M. W., Mitrovic, S., Fava, E., Silberberg, Y., Sharan, R., Zerial, M. and Hauri, H. P. (2010). MAPK signaling to the early secretory pathway revealed by kinase/phosphatase functional screening. *J. Cell Biol.* **189**, 997-1011.
Farías, G. G., Cuitino, L., Guo, X., Ren, X., Jarnik, M., Mattera, R. and Bonifacino, J. S. (2012). Signal-mediated, AP-1/clathrin-dependent sorting of transmembrane receptors to the somatodendritic domain of hippocampal neurons. *Neuron* **75**, 810-823.
Fields, I. C., King, S. M., Shteyn, E., Kang, R. S. and Fölsch, H. (2010). Phosphatidylinositol 3,4,5-trisphosphate localization in recycling endosomes is

necessary for AP-1B-dependent sorting in polarized epithelial cells. *Mol. Biol. Cell* **21**, 95-105.
Fiuza, M., González-González, I. and Pérez-Otaño, I. (2013). GluN3A expression restricts spine maturation via inhibition of GIT1/Rac1 signaling. *Proc. Natl. Acad. Sci. USA* **110**, 20807-20812.
Ganesan, A. K., Ho, H., Bodemann, B., Petersen, S., Aruri, J., Koshy, S., Richardson, Z., Le, L. Q., Krasieva, T., Roth, M. G. et al. (2008). Genome-wide siRNA-based functional genomics of pigmentation identifies novel genes and pathways that impact melanogenesis in human cells. *PLoS Genet.* **4**, e1000298.
Geiger, T., Wehner, A., Schaab, C., Cox, J. and Mann, M. (2012). Comparative proteomic analysis of eleven common cell lines reveals ubiquitous but varying expression of most proteins. *Mol. Cell. Proteomics* **11**, M111.014050.
Ghosh, P., Dahms, N. M. and Kornfeld, S. (2003). Mannose 6-phosphate receptors: new twists in the tale. *Nat. Rev. Mol. Cell Biol.* **4**, 202-213.
Hirokawa, N., Niwa, S. and Tanaka, Y. (2010). Molecular motors in neurons: transport mechanisms and roles in brain function, development, and disease. *Neuron* **68**, 610-638.
Hirst, J., Borner, G. H., Antrobus, R., Peden, A. A., Hodson, N. A., Sahlender, D. A. and Robinson, M. S. (2012). Distinct and overlapping roles for AP-1 and GGAs revealed by the ''knocksideways'' system. *Curr. Biol.* **22**, 1711-1716.
Kamentsky, L., Jones, T. R., Fraser, A., Bray, M. A., Logan, D. J., Madden, K. L., Ljosa, V., Rueden, C., Eliceiri, K. W. and Carpenter, A. E. (2011). Improved structure, function and compatibility for CellProfiler: modular high-throughput image analysis software. *Bioinformatics* **27**, 1179-1180.
Kim, S., Ko, J., Shin, H., Lee, J. R., Lim, C., Han, J. H., Altrock, W. D., Garner, C. C., Gundelfinger, E. D., Premont, R. T. et al. (2003). The GIT family of proteins forms multimers and associates with the presynaptic cytomatrix protein Piccolo. *J. Biol. Chem.* **278**, 6291-6300.
König, R., Chiang, C. Y., Tu, B. P., Yan, S. F., DeJesus, P. D., Romero, A., Bergauer, T., Orth, A., Krueger, U., Zhou, Y. et al. (2007). A probability-based approach for the analysis of large-scale RNAi screens. *Nat. Methods* **4**, 847-849.
Kozik, P., Hodson, N. A., Sahlender, D. A., Simecek, N., Soromani, C., Wu, J., Collinson, L. M. and Robinson, M. S. (2013). A human genome-wide screen for regulators of clathrin-coated vesicle formation reveals an unexpected role for the V-ATPase. *Nat. Cell Biol.* **15**, 50-60.
Kreis, P., Thévenot, E., Rousseau, V., Boda, B., Muller, D. and Barnier, J. V. (2007). The p21-activated kinase 3 implicated in mental retardation regulates spine morphogenesis through a Cdc42-dependent pathway. *J. Biol. Chem.* **282**, 21497-21506.
Lin, S. X., Mallet, W. G., Huang, A. Y. and Maxfield, F. R. (2004). Endocytosed cation-independent mannose 6-phosphate receptor traffics via the endocytic recycling compartment en route to the trans-Golgi network and a subpopulation of late endosomes. *Mol. Biol. Cell* **15**, 721-733.
Margeta, M. A., Wang, G. J. and Shen, K. (2009). Clathrin adaptor AP-1 complex excludes multiple postsynaptic receptors from axons in C. elegans. *Proc. Natl. Acad. Sci. USA* **106**, 1632-1637.
Mathews, P. M., Guerra, C. B., Jiang, Y., Grbovic, O. M., Kao, B. H., Schmidt, S. D., Dinakar, R., Mercken, M., Hille-Rehfeld, A., Rohrer, J. et al. (2002). Alzheimer's disease-related overexpression of the cation-dependent mannose 6-phosphate receptor increases Abeta secretion: role for altered lysosomal hydrolase distribution in beta-amyloidogenesis. *J. Biol. Chem.* **277**, 5299-5307.
McKenzie, J. E., Raisley, B., Zhou, X., Naslavsky, N., Taguchi, T., Caplan, S. and Sheff, D. (2012). Retromer guides STxB and CD8-M6PR from early to recycling endosomes, EHD1 guides STxB from recycling endosome to Golgi. *Traffic* **13**, 1140-1159.
McMahon, H. T. and Boucrot, E. (2011). Molecular mechanism and physiological functions of clathrin-mediated endocytosis. *Nat. Rev. Mol. Cell Biol.* **12**, 517-533.
Meyer, C., Zizioli, D., Lausmann, S., Eskelinen, E. L., Hamann, J., Saftig, P., von Figura, K. and Schu, P. (2000). mu1A-adaptin-deficient mice: lethality, loss of AP-1 binding and rerouting of mannose 6-phosphate receptors. *EMBO J.* **19**, 2193-2203.
Miserey-Lenkei, S., Chalancon, G., Bardin, S., Formstecher, E., Goud, B. and Echard, A. (2010). Rab and actomyosin-dependent fission of transport vesicles at the Golgi complex. *Nat. Cell Biol.* **12**, 645-654.
Mootha, V. K., Lindgren, C. M., Eriksson, K. F., Subramanian, A., Sihag, S., Lehar, J., Puigserver, P., Carlsson, E., Ridderstråle, M., Laurila, E. et al. (2003). PGC-1alpha-responsive genes involved in oxidative phosphorylation are coordinately downregulated in human diabetes. *Nat. Genet.* **34**, 267-273.
Moreau, D., Kumar, P., Wang, S. C., Chaumet, A., Chew, S. Y., Chevalley, H. and Bard, F. (2011). Genome-wide RNAi screens identify genes required for Ricin and PE intoxications. *Dev. Cell* **21**, 231-244.
Munier-Lehmann, H., Mauxion, F., Bauer, U., Lobel, P. and Hoflack, B. (1996a). Re-expression of the mannose 6-phosphate receptors in receptor-deficient fibroblasts. Complementary function of the two mannose 6-phosphate receptors in lysosomal enzyme targeting. *J. Biol. Chem.* **271**, 15166-15174.
Munier-Lehmann, H., Mauxion, F. and Hoflack, B. (1996b). Function of the two mannose 6-phosphate receptors in lysosomal enzyme transport. *Biochem. Soc. Trans.* **24**, 133-136.
Naughtin, M. J., Sheffield, D. A., Rahman, P., Hughes, W. E., Gurung, R., Stow, J. L., Nandurkar, H. H., Dyson, J. M. and Mitchell, C. A. (2010). The myotubularin phosphatase MTMR4 regulates sorting from early endosomes. *J. Cell Sci.* **123**, 3071-3083.
Orvedahl, A., Sumpter, R., Jr, Xiao, G., Ng, A., Zou, Z., Tang, Y., Narimatsu, M., Gilpin, C., Sun, Q., Roth, M. et al. (2011). Image-based genome-wide siRNA screen identifies selective autophagy factors. *Nature* **480**, 113-117.
Park, H. and Poo, M. M. (2013). Neurotrophin regulation of neural circuit development and function. *Nat. Rev. Neurosci.* **14**, 7-23.
Pfeffer, S. R. (2007). Unsolved mysteries in membrane traffic. *Annu. Rev. Biochem.* **76**, 629-645.
Popoff, V., Mardones, G. A., Tenza, D., Rojas, R., Lamaze, C., Bonifacino, J. S., Raposo, G. and Johannes, L. (2007). The retromer complex and clathrin define an early endosomal retrograde exit site. *J. Cell Sci.* **120**, 2022-2031.
Port, F. and Basler, K. (2010). Wnt trafficking: new insights into Wnt maturation, secretion and spreading. *Traffic* **11**, 1265-1271.
Prasad, T. S., Kandasamy, K. and Pandey, A. (2009). Human Protein Reference Database and Human Proteinpedia as discovery tools for systems biology. *Methods Mol. Biol.* **577**, 67-79.
Roberts, R., Sciorra, V. A. and Morris, A. J. (1998). Human type 2 phosphatidic acid phosphohydrolases. Substrate specificity of the type 2a, 2b, and 2c enzymes and cell surface activity of the 2a isoform. *J. Biol. Chem.* **273**, 22059-22067.
Saini, D. K., Karunarathne, W. K., Angaswamy, N., Saini, D., Cho, J. H., Kalyanaraman, V. and Gautam, N. (2010). Regulation of Golgi structure and secretion by receptor-induced G protein βγ complex translocation. *Proc. Natl. Acad. Sci. USA* **107**, 11417-11422.
Sarri, E., Sicart, A., Lázaro-Diéguez, F. and Egea, G. (2011). Phospholipid synthesis participates in the regulation of diacylglycerol required for membrane trafficking at the Golgi complex. *J. Biol. Chem.* **286**, 28632-28643.
Scott, G. K., Fei, H., Thomas, L., Medigeshi, G. R. and Thomas, G. (2006). A PACS-1, GGA3 and CK2 complex regulates CI-MPR trafficking. *EMBO J.* **25**, 4423-4435.
Simpson, J. C., Joggerst, B., Laketa, V., Verissimo, F., Cetin, C., Erfle, H., Bexiga, M. G., Singan, V. R., Hériché, J. K., Neumann, B. et al. (2012). Genome-wide RNAi screening identifies human proteins with a regulatory function in the early secretory pathway. *Nat. Cell Biol.* **14**, 764-774.
Smyth, S. S., Sciorra, V. A., Sigal, Y. J., Pamuklar, Z., Wang, Z., Xu, Y., Prestwich, G. D. and Morris, A. J. (2003). Lipid phosphate phosphatases regulate lysophosphatidic acid production and signaling in platelets: studies using chemical inhibitors of lipid phosphate phosphatase activity. *J. Biol. Chem.* **278**, 43214-43223.
Snel, B., Lehmann, G., Bork, P. and Huynen, M. A. (2000). STRING: a web-server to retrieve and display the repeatedly occurring neighbourhood of a gene. *Nucleic Acids Res.* **28**, 3442-3444.
Subramanian, A., Tamayo, P., Mootha, V. K., Mukherjee, S., Ebert, B. L., Gillette, M. A., Paulovich, A., Pomeroy, S. L., Golub, T. R., Lander, E. S. et al. (2005). Gene set enrichment analysis: a knowledge-based approach for interpreting genome-wide expression profiles. *Proc. Natl. Acad. Sci. USA* **102**, 15545-15550.
Szklarczyk, D., Franceschini, A., Kuhn, M., Simonovic, M., Roth, A., Minguez, P., Doerks, T., Stark, M., Muller, J., Bork, P. et al. (2011). The STRING database in 2011: functional interaction networks of proteins, globally integrated and scored. *Nucleic Acids Res.* **39**, D561-D568.
Tarpey, P. S., Stevens, C., Teague, J., Edkins, S., O'Meara, S., Avis, T., Barthorpe, S., Buck, G., Butler, A., Cole, J. et al. (2006). Mutations in the gene encoding the Sigma 2 subunit of the adaptor protein 1 complex, AP1S2, cause X-linked mental retardation. *Am. J. Hum. Genet.* **79**, 1119-1124.
Vicente-Manzanares, M., Ma, X., Adelstein, R. S. and Horwitz, A. R. (2009). Non-muscle myosin II takes centre stage in cell adhesion and migration. *Nat. Rev. Mol. Cell Biol.* **10**, 778-790.
Vicinanza, M., D'Angelo, G., Di Campli, A. and De Matteis, M. A. (2008). Function and dysfunction of the PI system in membrane trafficking. *EMBO J.* **27**, 2457-2470.
Waguri, S., Dewitte, F., Le Borgne, R., Rouillé, Y., Uchiyama, Y., Dubremetz, J. F. and Hoflack, B. (2003). Visualization of TGN to endosome trafficking through fluorescently labeled MPR and AP-1 in living cells. *Mol. Biol. Cell* **14**, 142-155.
Waguri, S., Tomiyama, Y., Ikeda, H., Hida, T., Sakai, N., Taniike, M., Ebisu, S. and Uchiyama, Y. (2006). The luminal domain participates in the endosomal trafficking of the cation-independent mannose 6-phosphate receptor. *Exp. Cell Res.* **312**, 4090-4107.
Wassmer, T., Attar, N., Bujny, M. V., Oakley, J., Traer, C. J. and Cullen, P. J. (2007). A loss-of-function screen reveals SNX5 and SNX6 as potential components of the mammalian retromer. *J. Cell Sci.* **120**, 45-54.
Watanabe, T., Hosoya, H. and Yonemura, S. (2007). Regulation of myosin II dynamics by phosphorylation and dephosphorylation of its light chain in epithelial cells. *Mol. Biol. Cell* **18**, 605-616.
Wilkinson, S., Paterson, H. F. and Marshall, C. J. (2005). Cdc42-MRCK and Rho-ROCK signalling cooperate in myosin phosphorylation and cell invasion. *Nat. Cell Biol.* **7**, 255-261.
Yamada, A., Mamane, A., Lee-Tin-Wah, J., Di Cicco, A., Prévost, C., Lévy, D., Joanny, J. F., Coudrier, E. and Bassereau, P. (2014). Catch-bond behaviour facilitates membrane tubulation by non-processive myosin 1b. *Nat. Commun.* **5**, 3624.
Zhang, H., Webb, D. J., Asmussen, H., Niu, S. and Horwitz, A. F. (2005). A GIT1/PIX/Rac/PAK signaling module regulates spine morphogenesis and synapse formation through MLC. *J. Neurosci.* **25**, 3379-3388.